PAPER

CrossMark
click for updates

Zn-modified ceria as a redox material for thermochemical H_2O and CO_2 splitting: effect of a secondary ZnO phase on its thermochemical activity†

Fangjian Lin,[a] Vallerie A. Samson,[b] Andrea O. Wismer,[a] Daniel Grolimund,[b] Ivo Alxneit[*a] and Alexander Wokaun[c]

Two-step thermochemical cycles based on ceria (CeO_2) are a promising way to store dilute and intermittent solar energy by producing chemical fuels (solar fuels) such as H_2 and CO from H_2O and CO_2 with concentrated solar radiation. Many studies have shown that the fuel yield per cycle can be enhanced by introducing certain heterocations (dopants) into the ceria lattice. In this study, dual-phase Zn-modified ceria synthesized by coprecipitation was investigated as a redox material for thermochemical H_2O and CO_2 splitting. Surprisingly, the material exhibits significant increase of the H_2 and CO productivities during the first few cycles, in contrast to an anticipated decrease of activity due to sintering. Data suggests that the material's solar fuel productivity eventually stabilizes and exceeds that of native ceria. To elucidate the cause of this observation, changes of the material's physicochemical properties during the initial cycles were analysed in detail. The chemical compositions and elemental distribution were probed using X-ray fluorescence (XRF) spectroscopy with lab and synchrotron X-ray sources. The observed increase of productivity during the initial cycles is correlated with a significant loss of zinc through ZnO sublimation, suggesting a negative effect of the secondary ZnO phase in Zn-modified ceria for its thermochemical activity. Structural changes were revealed by synchrotron micro X-ray powder diffraction (μ-XRD) and X-ray absorption spectroscopy (XAS). The zinc that remains incorporated in the ceria lattice after the initial cycles is likely to be responsible for its higher thermochemical activity in comparison to native ceria.

Introduction

Largely driven by economic and population growth, the world's energy demand is projected to continue to increase in the foreseeable future.[1,2] The risk of long-term adverse climate changes due to increasing fossil fuel consumption demands a transition of the energy supply to clean and renewable energy sources. Despite its abundance, solar energy is difficult to use at a large scale because it is intermittent and dilute. For it to become a major primary

energy source, it needs to be converted and stored as transportable energy carriers that are available when and where needed.

The storage of solar energy in the form of chemical bonds in so-called solar fuels is arguably one of the most attractive approaches. One promising path for solar fuel generation is solar-driven thermochemical cycles (STCs). In a typical two-step STC, as illustrated in Fig. 1, high temperatures generated by concentrated solar radiation drive the endothermic activation of a metal oxide. During activation, the material is reduced and O_2 is released. Depending on reaction temperature and the oxide used, the oxide is reduced either to the corresponding metal, or to a lower valent oxide, or to a nonstoichiometric phase. In the second step, typically performed at lower temperatures, the reduced material is reoxidized by $H_2O_{(g)}$ or CO_2. H_2 or CO is produced as a result and the material is converted to its original oxidized state. Syngas, a mixture of H_2 and CO, is produced if $H_2O_{(g)}$ and CO_2 are used simultaneously. The chemical yield, *i.e.* the amount of H_2 or CO produced in one cycle per unit of oxide material, depends largely on the degree of reduction achieved during the

[a] *Solar Technology Laboratory, Paul Scherrer Institute, CH-5232 Villigen PSI, Switzerland. E-mail: ivo.alxneit@psi.ch; Fax: +41 56 310 2688; Tel: +41 56 310 4092*
[b] *microXAS Beamline, Swiss Light Source, Paul Scherrer Institute, CH-5232 Villigen PSI, Switzerland*
[c] *General Energy Research Department, Paul Scherrer Institute, CH-5232 Villigen PSI, Switzerland*
† Electronic supplementary information (ESI) available: Comparison of H_2 evolution profiles between materials, ion current profiles of H_2 and O_2 for extended cycling, cerium distribution, overview XRF maps for synchrotron X-ray characterization, and XRD patterns with conventional X-ray. See DOI: 10.1039/c6ce00430j
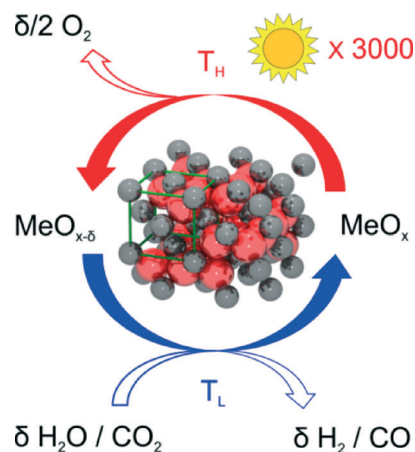
Fig. 1 Schematic illustration of two-step solar-driven thermochemical cycles based on a metal oxide (MeO_x) for syngas (H_2 and CO) production. The lattice in the centre of the figure represents a fluorite-type oxide (*e.g.* ceria).

activation (assuming full reoxidation). The complete process can be summarized as follows.
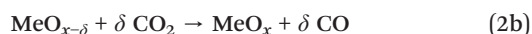
Thermal reduction at a high temperature (T_H)

$$MeO_x \rightarrow MeO_{x-\delta} + \delta/2\ O_2 \qquad (1)$$
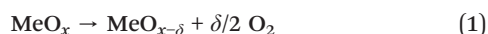
Reoxidation with H_2O at a low temperature (T_L)

$$MeO_{x-\delta} + \delta\ H_2O \rightarrow MeO_x + \delta\ H_2 \qquad (2a)$$
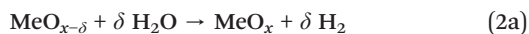
Reoxidation with CO_2 at a low temperature (T_L)

$$MeO_{x-\delta} + \delta\ CO_2 \rightarrow MeO_x + \delta\ CO \qquad (2b)$$

Reactions 1 and 2a (or 2b) result in H_2O (or CO_2) splitting as the net reaction 3a (or 3b) in a cycle, with inherent temporal separation of the H_2 (or CO) produced and the O_2 evolved.

$$H_2O \rightarrow H_2 + 1/2\ O_2 \qquad (3a)$$

$$CO_2 \rightarrow CO + 1/2\ O_2 \qquad (3b)$$

The state-of-the-art redox materials for two-step STCs are mainly non-stoichiometric metal oxides such as perovskites and ceria (CeO_2). Perovskite-type oxides have emerged very recently as promising candidates for STCs due to their potential for relatively low temperature operation and high oxygen storage capacities.[3–11] Increased fuel production, however, comes at the price of slower reoxidation rates due to reduced thermodynamic driving force.[3,8,12,13] Partly owing to its fast reoxidation kinetics, ceria remains arguably the most promising metal oxide for two-step STCs.[14–18] The feasibility of STCs with ceria under realistic concentrated solar radiation and process conditions was demonstrated by Chueh *et al.* using a cavity-receiver reactor.[15] In attempt to increase the fuel yield per cycle, ceria doped with various metal cations has been extensively investigated with various degrees of success.[19–30] A

notable example is Zr-doped ceria, which was shown to increase solar fuel production,[12,22,24,25,27–29] but again at the price of slower reoxidation rates. The incorporation of trivalent lanthanide cations (La, Sm and Gd) did not result in a better performance than native ceria, according to Le Gal *et al.*[23,25] However, the addition of La or Gd to Zr-doped ceria resulted in an increased thermal stability.[23,25] Studies on ceria doped with alkaline metal cations have also been reported. The activity of $Ce_{0.9}M_{0.1}O_{2-\delta}$ (M = Mg, Ca, Sr, Sc, Y, Dy, Zr and Hf) for thermochemical H_2O splitting was investigated by Meng *et al.*[30] Only Zr-, Hf-, and Sc-doped ceria exhibited larger H_2 yield compared to native ceria.[30] Scheffe *et al.* also observed an enhanced CO_2-splitting activity with Zr- and Hf-doped ceria.[27] In contrast, two recent studies by Kang *et al.* show that the addition of the alkaline earth metal cations Ca^{2+} and Mg^{2+} into the lattice of ceria–zirconia oxide promotes its thermochemical activity for CO_2 splitting.[28,29]

Contradictory results on the effect of the same dopant on ceria's thermochemical activity can be found in the literature. This could be due to the differences in the exact synthesis procedures and thermochemical reaction conditions used in different studies. The studies mentioned previously illustrate the complex role of the dopants in modifying ceria's activity for STCs, which in many cases remains to be fully understood. In many of these studies, the focus was on screening different dopants, *i.e.* the evaluation of the material's thermochemical activity. Very often, the material's activity quickly decreases during the initial cycles due to a number of reasons including sintering and physicochemical changes at high temperatures. However, very few studies attempt to monitor chemical and structural changes of the materials despite their importance in understanding the material's activity and the changes of the activity during these initial cycles.

In this study, we present a study of Zn-modified ceria for thermochemical H_2O and CO_2 splitting with an emphasis on the changes of the material's physicochemical properties during multiple cycles. This material is chosen partly because Zn-modified ceria, as a catalyst or a support oxide for gold nanoparticles, exhibits enhanced catalytic activity for CO oxidation in comparison to native ceria.[31–33] In addition, the material used in this study has been well characterized previously with a number of standard and advanced techniques.[34,35] The material exhibits nearly twice the oxygen storage capacity (OSC) of native ceria and shows superior activity for the reverse water-gas shift reaction (CO_2-to-CO conversion in presence of H_2),[35] indicating its potential for STCs. We show in this study a unique, counter-intuitive behaviour of Zn-modified ceria as a redox material for solar-driven thermochemical H_2O and CO_2 splitting: the H_2 and CO productivities increase significantly during the first few cycles, and eventually stabilize and exceed those of native ceria. The concomitant physicochemical changes are elucidated using X-ray fluorescence spectroscopy with lab and synchrotron X-ray sources. Structural changes are revealed by synchrotron X-ray powder diffraction and X-ray absorption spectroscopy. This study, together with our previous studies of the same

material,[34,35] underlines the necessity and importance of understanding the structural and chemical stability of a material at conditions relevant to STCs, if a catalyst designed for reactions at low-to-moderate temperatures is considered as a redox material for STCs.

Experimental

Synthesis

Zn-modified ceria (nominal molar fraction X_{Zn} = 0.1 and 0.2, balance Ce) used in this study was synthesized by coprecipitation and from the same batch as the material used in a previous study.[35] The exact synthesis procedure can be found in an earlier publication.[34] Briefly, appropriate quantities of the cerium and zinc nitrate precursors were dissolved in excess amount of deionized water. Upon complete dissolution, precipitation was induced by the addition of dilute aqueous ammonia solution under vigorous stirring until the pH of the solution stabilized at 10. After ageing under stirring for 24 h, the precipitate was allowed to settle for another day. The precipitate was filtered and rinsed several times using a Büchner funnel. The filter cake was then dried and crushed into fine powders before being calcined in air for 5 h at 500 °C. The obtained materials are designated as 10Zn and 20Zn. Native ceria was synthesized following the same procedure except at pH = 9.

Thermochemical activity

Thermochemical H_2O-splitting experiments with native ceria, 10Zn and 20Zn were carried out using a home-built setup. The setup consists of three major components: a gas supply system with a two-position valve to switch between different atmospheres, an alumina tube reactor housed in a programmable tube furnace, and a gas analysis system consisting of a mass spectrometer (MS) and a gas chromatograph (GC). Unreacted water was removed in a cold-trap between the reactor and the gas analysis system. The thermal reduction was carried out at about 1290 °C in Ar at a flow rate of 80 Nml min^{-1}. The reoxidation was performed under a mixture of Ar at 80 Nml min^{-1} and $H_2O_{(g)}$ at 1 g h^{-1} (equivalent to 20.7 Nml min^{-1}). About 250 mg of Zn-modified ceria was used in each test. The concentration of the H_2 evolved was continuously monitored by the MS at a time resolution of a few seconds.

Thermochemical CO_2-splitting experiments were carried out using a thermogravimetric analyser (TGA, Netzsch TA409). About 200 mg of sample was loaded in an alumina crucible. The gas flow was maintained at 100 Nml min^{-1} for all measurements. The sample was heated to either 1300 °C or 1400 °C at a rate of 30 °C min^{-1} under Ar. The temperature was maintained for 45 min, during which the material was thermally reduced. After cooling to 1000 °C at a rate of 30 °C min^{-1}, the atmosphere was changed to 25 vol% CO_2 balanced with Ar and the sample was reoxidized for 15 min. Four cycles were repeated for each sample at the two reduction temperatures. Starting with the second cycle, the heating

rate was decreased to 20 °C min^{-1}. The effluent gas was monitored by GC and MS. A blank was measured to compensate buoyancy effects. The specific CO production was estimated from the relative mass gain (%) recorded by the TGA.

Standard characterization

Crystalline phases of selected materials after reaction were identified by a PANalytical X'Pert X-ray powder diffractometer (results presented in the ESI†). It was operated in continuous scanning mode with Cu K_α radiation (λ = 1.5405 Å) at 45 kV and 20 mA. An integration time of 5 s and a step size of 0.05° were used for all measurements. The samples were prepared by depositing slurry of finely ground powder in ethanol on clean glass substrates.

The chemical changes of the materials undergoing different number of H_2O-splitting cycles were investigated by X-ray fluorescence (XRF) spectroscopy with a micro X-ray fluorescence analyser (EDAX ORBIS) equipped with a rhodium anode. The characteristic X-ray fluorescence from the samples was detected by a solid-state multi-channel photon detector. The instrument was operated at 35 kV and 400 μA. A beam diameter of 2 mm was chosen to collect spectra representing the average sample composition and the collection time was set to 100 s. For elemental mapping a beam diameter of 30 μm and a dwell time of 300 ms were chosen.

Synchrotron X-ray characterization

To elucidate the structural changes, materials subjected to different number of H_2O-splitting cycles were characterized using spatially-resolved synchrotron micro X-ray powder diffraction (μ-XRD) and X-ray absorption spectroscopy (XAS), both coupled with μ-XRF. The combination of these techniques allows the identification of potential trace phases within the materials, the structural changes during the initial cycles, and potential structural inhomogeneity within a chemically inhomogeneous sample. The characterization was carried out at the microXAS beamline of the Swiss Light Source. Samples were prepared by pressing pellets out of a mixture of finely ground sample powder and a hydrocarbon-based binder. For μ-XRF and μ-XRD studies, monochromatic X-ray of 10 keV was focused by a Kirkpatrick–Baez mirror system to a beam size of approximately 5 × 5 μm². The fluorescence photons from the irradiated sample were detected with a Ketek Si side-drift detector (SDD) at an angle of approximately 90° to the incoming X-ray beam. The sample was mounted vertically on a motorized sample stage that allows its displacement on three axes with sub-micrometer resolution. Combined with a micro-sized beam, high-resolution mapping of the chemical compositions can be achieved. Typically, an overview of the cerium and zinc elemental distribution was recorded first. Two regions of interest were then selected for high resolution mapping with a longer dwell time and higher spatial resolution. A Pilatus area detector was positioned behind the sample to record simultaneously the μ-diffraction patterns (4 s of integration time per pattern).

The same setup was used to collect XAS data in fluorescence mode. Unless indicated otherwise, a big-beam configuration was used for XAS measurements. The XAS spectrum reported for a given sample is the sum of typically 10 to 20 individual spectra collected repeatedly.

Results and discussion

Thermochemical H_2O splitting

In Fig. 2 H_2 evolution profiles of native ceria and Zn-modified materials (10Zn and 20Zn) during four consecutive H_2O-splitting cycles are presented. It is obvious from Fig. 2a that native ceria exhibits a stable H_2O-splitting activity during the four cycles. Constant peak H_2 concentrations of about 1000 ppm (0.1%) are observed. In contrast, increasing H_2 peak concentrations are observed for both Zn-modified samples (Fig. 2b and c). This seems counter-intuitive, as one generally expects some loss of activity due to materials sintering at high temperatures. While the peak H_2 concentrations observed for 10Zn and 20Zn are significantly lower in the first two cycles, they increase to levels that are only slightly lower than that of native ceria in cycles #3 and #4 (also see Fig. S1†). In addition, compared to that of native ceria, the H_2 evolution profiles of the Zn-modified ceria samples suggest slightly slower reoxidation rates. The peak concentrations are reached later and hydrogen evolution seems to continue at a rather low level for longer time (Fig. S1†). Slower reoxidation due to the incorporation of heterocations, in this case Zn^{2+}, is consistent with previous reports on thermochemical cycles using ceria doped with other metal cations.[12,22,27] O_2 evolution was not detected during the thermal reduction steps of this particular experiment, as the raw data of O_2 ion currents unexpectedly showed no values. To verify whether the H_2 evolution with the Zn-modified ceria samples truly stabilizes after four cycles, and to gain information on the evolution of O_2, the experiment was repeated for 6 H_2O-splitting cycles, and the ion currents were recorded directly. Clearly, the increase of the peak H_2 concentrations as well as its stabiliza-

tion after about 3 to 4 cycles observed in Fig. 2 could be reproduced for both 20Zn (Fig. S2†) and 10Zn (Fig. S3†). In contrast to the significant increase of the H_2 signal, the O_2 signal only increases slightly during the initial cycles for both samples. For its cause, further investigation is required.

Taking into account the known gas flow rate and the mass of the sample used, integration of the H_2 evolution profiles of Fig. 2 results in the amounts of H_2 produced per unit sample mass. The results are presented in Fig. 3. The average amount of H_2 produced for native ceria is 52.0 ($\pm$3.8) $\mu mol\ g^{-1}$ per cycle. For 10Zn, the amount increases from 20.8 $\mu mol\ g^{-1}$ in the first cycle to 57.6 $\mu mol\ g^{-1}$ in the 4th cycle, while for 20Zn, the amount increases from 19.5 $\mu mol\ g^{-1}$ to 62.0 $\mu mol\ g^{-1}$. These values are generally in agreement with the results obtained in an earlier study.[36] Interestingly, while the H_2O-splitting activity seems to start stabilizing in cycle #4 for both 20Zn and 10Zn, the amounts of H_2 produced are consistently higher than the average value of native ceria. This is tentatively attributed to the increased OSC of Zn-modified ceria as revealed by our previous study.[35] The large increase in the amount of H_2 produced observed for both Zn-modified samples indicates physicochemical changes of the materials during the initial four cycles.

Characterization after H_2O splitting

To shed light on the marked increase of H_2 productivities in the first four cycles, the distribution and amounts of zinc and cerium in 20Zn and 10Zn after the 1st, 2nd and 4th cycle were measured with the micro XRF analyser. The results are presented in Fig. 4. 10Zn (Fig. 4a) and 20Zn (Fig. 4b) clearly exhibit an inhomogeneous distribution of zinc. This observation is consistent with the results of an earlier study in which the material was subjected to high temperature annealing in air.[34] Cerium, however, is distributed homogeneously after four cycles according to XRF mapping (Fig. S4†). In addition, evident from the color change (towards blue) of the maps in Fig. 4a and b, the average concentration of zinc in both samples decreases dramatically with increasing number of cycles. Thus, large loss of zinc occurs initially. A quantitative
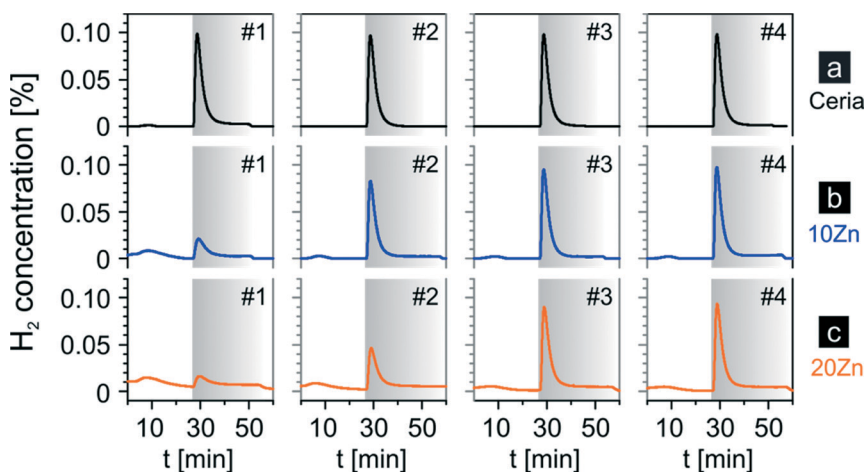

Fig. 2 H_2 evolution profiles of (a) native ceria, (b) 10Zn, and (c) 20Zn for 4 H_2O-splitting cycles. Thermal reduction was carried out at about 1290 °C and reoxidation (grey region) at 1000 °C.
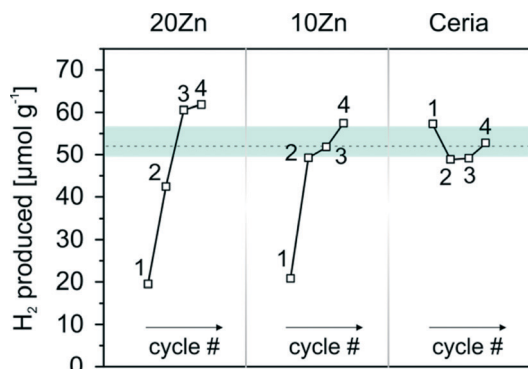
Fig. 3 Comparison of H_2 productivity at 1000 °C by native ceria, 10Zn, and 20Zn during 4 H_2O-splitting cycles. The colored band indicates the range of native ceria's productivities and the dashed line indicates the average value.
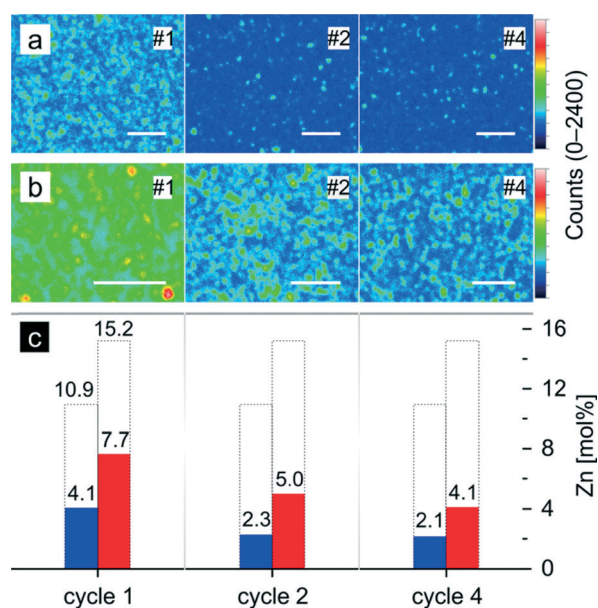

Fig. 4 Zinc XRF maps of (a) 10Zn and (b) 20Zn after 1, 2 and 4 H_2O-splitting cycles. The scale in each map represents a length of 500 μm. Corresponding average zinc concentrations (blue: 10Zn, red: 20Zn) are presented in (c). The concentrations of zinc in the starting materials (bars with dashed lines) are included for comparison.

evaluation of the XRF data is presented in Fig. 4c. For 10Zn, the starting material contains 10.9 mol% zinc (balance cerium). This value is close to the nominal 10 mol% and the value measured by ICP-OES reported earlier.[34] However, for 20Zn, according to XRF only about 15 mol% zinc is present in 20Zn (nominal 20 mol%), which again is consistent with the ICP-OES results showing a significantly lower zinc content. Approximately half of the zinc is lost after the first H_2O-splitting cycle for 20Zn and more than 60% for 10Zn. After four cycles, the zinc concentration reaches 4.1 mol% in 20Zn and 2.1 mol% in 10Zn, close to the solubility limit of ZnO in CeO_2 of 3.1 ± 0.7 mol% reported by Schmale et al.[37] From our previous study,[34] we know that substantial amounts of zinc are present as non-incorporated X-ray amorphous ZnO

in the Zn-modified ceria samples after synthesis (calcined at 500 °C). The observed loss of zinc during the initial cycles is attributed to the sublimation of this secondary ZnO phase at the thermal reduction temperature in a flow of inert gas. This has been confirmed by CO_2-splitting experiments that will be presented later. The loss of zinc during these cycles (Fig. 4c) by ZnO sublimation correlates with the gradual increase of H_2 productivity (Fig. 3), suggesting an adverse effect of the secondary ZnO phase on ceria's thermochemical activity.

To better understand the higher activity of Zn-modified ceria in the 4th cycle with respect to the average of native ceria, insights into the structural characteristics of the cycled materials are desired. The materials (10Zn and 20Zn) after 4 H_2O-splitting cycles were characterized by synchrotron μ-XRD coupled with μ-XRF. As discussed earlier in the experimental section, these techniques allow the identification of crystalline phases including trace phases, and the determination of potential structural inhomogeneity existing in the chemically inhomogeneous Zn-modified ceria samples. Insights into local phase composition with corresponding chemical composition can be obtained.

To gain an overview of the element distribution, XRF maps of cerium and zinc for 10Zn ($\sim$300 $\times$ 300 μm²) and 20Zn ($\sim$200 $\times$ 200 μm²) after 4 H_2O-splitting cycles were recorded (see Fig. S5†). The inhomogeneities observed in both of the cerium maps are due to the presence of the organic binder that causes an uneven dilution of the samples. Note that samples used for Fig. S4† (and Fig. 4) were not mixed with the binder. The distribution of zinc, however, is much more inhomogeneous (Fig. S5b†), which cannot be attributed to imperfect mixing of the samples with the binder. The higher inhomogeneities observed in the zinc maps compared to those in the cerium maps are caused by inhomogeneous distribution of zinc.

Based on the overview maps, two regions of interest (marked in Fig. S5†), one Ce-rich and one Zn-rich, were selected for both samples. Fig. 5 presents the μ-diffraction patterns of these regions for 10Zn and 20Zn. Higher resolution μ-XRF maps of cerium and zinc of the selected regions are also included in the figure. For the same element of each sample, the two maps from the two regions are plotted in the same color scale. This allows direct comparison of the relative concentrations of cerium or zinc in the two regions. Thus the regions of a1 and b1 in Fig. 5 represent Ce-rich regions for 10Zn and 20Zn, respectively, and the regions of a2 and b2 represent Zn-rich regions. Each of the four regions was characterized by μ-XRD at a resolution of 5 $\times$ 5 μm², yielding hundreds of diffraction patterns. The diffraction patterns reported in Fig. 5 correspond to the sum of the patterns recorded for each of the four regions. Plotted in a logarithmic scale, trace phases are more likely to be visible. It is clear from the 2D diffraction patterns that in all regions the main phase (rings marked by black dots) is the cubic ceria phase. A second phase, marked by red dots and identified as wurzite ZnO, is also observed in all four regions. Comparing the relative intensities of the two phases, it is evident that
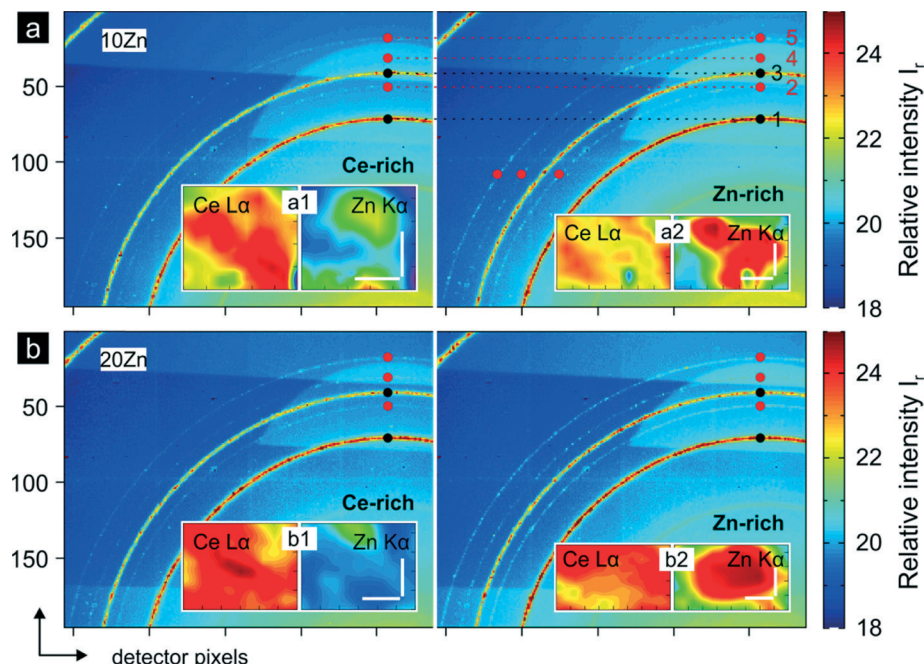
Fig. 5 Synchrotron 2D μ-XRD patterns of (a) 10Zn and (b) 20Zn after 4 H_2O-splitting cycles. Left column: patterns for Ce-rich regions (a1, b1). Right column: patterns for Zn-rich regions (a2, b2). The insets show corresponding cerium and zinc XRF maps of the regions, with scale bars all representing a length of 20 μm. Black dots "1" and "3" represent CeO_2 (111) and (200). Red dots "2", "4" and "5" represent ZnO (100), (002) and (101), respectively. The relative diffraction intensity (I_r) shown in the figure is the logarithm (base 2) of the intensity counts.

only trace amounts of ZnO are present. The ZnO phase is clearly more discernible in the Zn-rich region for 10Zn and for 20Zn. Comparing 20Zn with 10Zn, one finds that more ZnO is present in 20Zn. This is expected as the amount of zinc in 20Zn is twice the amount in 10Zn after 4 H_2O-splitting cycles (Fig. 4c). With standard XRD using conventional X-rays, ZnO could be barely detected after one or two cycles but not after four cycles (Fig. S6†).

Now it is evident that minor amounts of ZnO exist in the Ce-rich and Zn-rich regions of both samples after 4 H_2O-splitting cycles. To determine whether some zinc remain incorporated in the ceria lattice at this point, the four 2D diffraction patterns presented in Fig. 5 were azimuthally integrated to yield 1D patterns. The results are presented in Fig. 6. Wurzite ZnO (101) with a known inter-plane distance of 2.4759 Å was used as internal reference. This distance corresponds to a 2θ angle of 29° (see inset of Fig. 6), with an X-ray wavelength of 1.2398 Å (10 keV photon energy). Looking at the aligned 1D diffraction patterns of the two samples, one notices that the ceria peaks of 20Zn are at higher 2θ angles compared to 10Zn. This indicates that the lattice of 20Zn is contracted relative to the one of 10Zn. As known from our previous study,[34] the lattice of ceria contracts upon incorporation of zinc. Thus one can infer that more zinc is still incorporated in the ceria lattice of 20Zn compared to 10Zn after 4 H_2O-splitting cycles. Within the same sample, the ceria peaks coincide in Zn-rich and Ce-rich regions. This indicates a homogeneous substitution of cerium by zinc in the ceria lattice. Thus, the inhomogeneity of the zinc distribution observed after four cycles (Fig. 4)

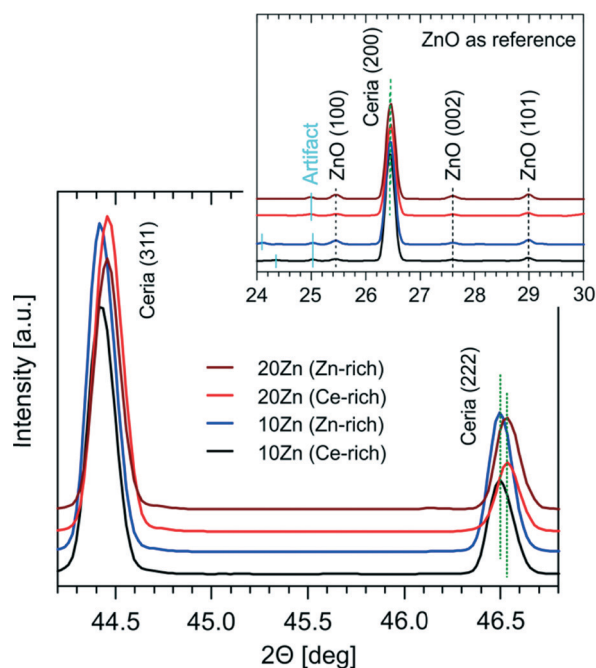reflects an inhomogeneous distribution of the secondary ZnO phase.

Fig. 6 1D diffraction patterns of Zn-rich and Ce-rich regions for 20Zn and 10Zn after 4 H_2O-splitting cycles. They were obtained by azimuthal integration of the 2D patterns presented in Fig. 5. The expected position of ZnO (101) at 2θ = 29° was used as internal reference to align the patterns (see inset).

The short-range local coordination environment of zinc in the fresh and reacted samples was investigated with Zn K-edge X-ray absorption spectroscopy (XAS). The XANES (X-ray absorption near edge structure) spectra and Fourier transformed (FT) EXAFS (extended X-ray absorption fine structure) spectra of fresh 20Zn and 10Zn are reported in Fig. 7a and c. Also included in the figures are the published spectra of ZnO particles with two very different sizes.[38,39] It is evident that the shape of the zinc 1s → 4p absorption (white line) strongly depends on the particle size. The white line shifts towards higher photon energies as the particle size increases. The shape of the XANES spectra of fresh 10Zn and 20Zn closely resemble the one of ZnO nanoparticles with a diameter of 2.1 nm. At higher energies only weak oscillations almost identical to the ones for the nanoparticles (2.1 nm) are observed, indicating local disorder around zinc in the fresh samples. A small shift of the white line energy to higher values and a slight increase of the oscillation amplitude is noticed when the XANES spectrum of 20Zn is compared to the one of 10Zn. This could be interpreted as slightly higher crystallinity of the ZnO phase in 20Zn than in 10Zn, although many factors including particle sizes and self-absorption may play a role in

determining the general shape and oscillation amplitude of an XANES spectrum.[40] However, a previous XRD study of the same materials shows a very weak reflection indicative of ZnO for 20Zn but not for 10Zn,[35] supporting this interpretation. The high disorder around zinc in the starting (fresh) materials is confirmed by their FT EXAFS spectra reported in Fig. 7c. The contribution of the second coordination shell (Zn–Zn coordination) is very small as judged from its FT magnitude. The EXAFS spectrum of large ZnO particles corresponds to a homogeneous and well crystallized material as several coordination shells can be identified. These XANES and EXAFS spectra strongly support the findings of our earlier study: X-ray amorphous ZnO exists in 10Zn and 20Zn after synthesis (calcined at 500 °C).[34]

Samples of 10Zn and 20Zn after one and after 4 H_2O-splitting cycles were also characterized by XAS. Selected results are presented in Fig. 7b and d. Three spectra are reported here: 10Zn after one H_2O-splitting cycle, 10Zn after four cycles measured with a large beam probing the average sample composition, and 10Zn after four cycles measured with the micro beam probing the centre of a Zn-rich region. It is evident from both the XANES and the EXAFS spectra that rapid
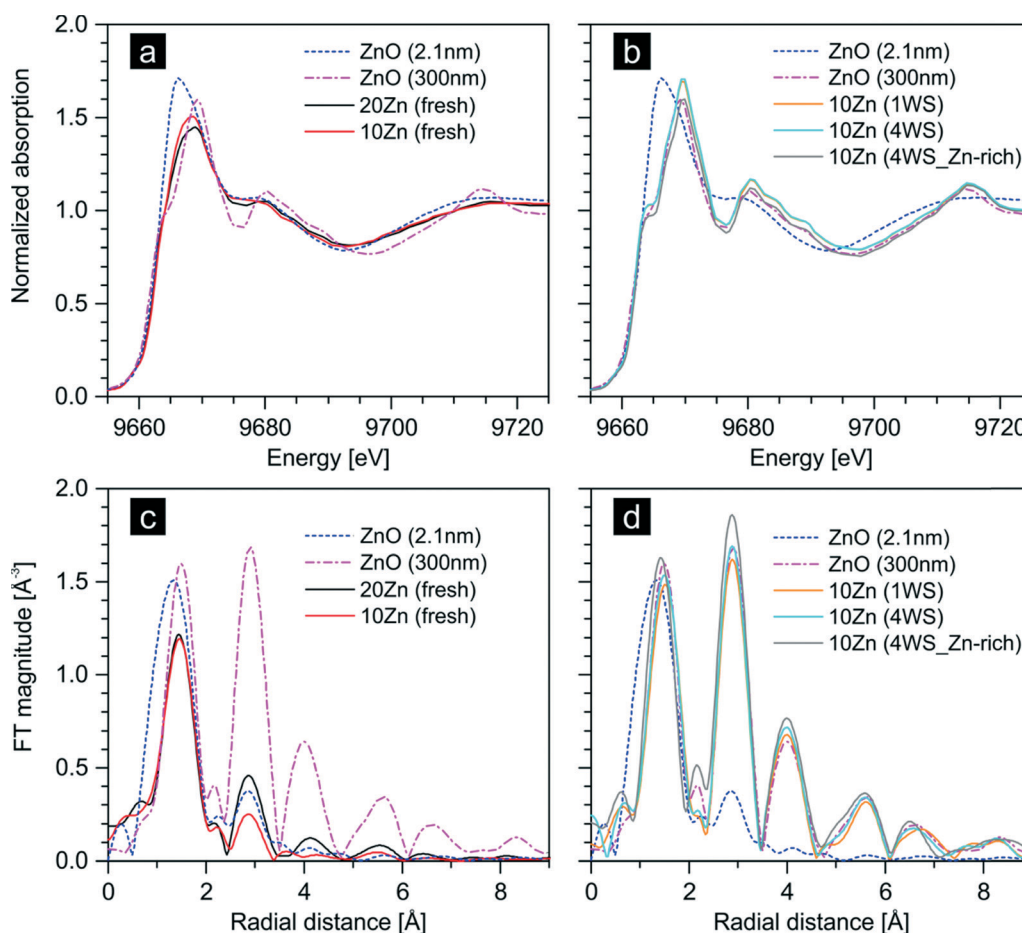

Fig. 7 XANES (a, b) and Fourier transformed EXAFS (c, d) spectra of fresh 10Zn and 20Zn, and 10Zn after 1 or 4 H_2O-splitting (WS) cycles. All the spectra were collected using big-beam configuration except for "10Zn (4WS_Zn-rich)", which was collected with a micro-sized beam in a typical Zn-rich region of 10Zn after four cycles. The spectra of X-ray amorphous ZnO (2.1 nm) and crystalline bulk ZnO (300 nm) are obtained from previous publications.[38,39]

sintering of ZnO occurs already during the first H_2O-splitting cycle. The XANES and EXAFS spectra of 10Zn after one H_2O-splitting cycle closely match the spectra of the 300 nm ZnO particles. In addition, these spectra after one cycle essentially overlap with the ones measured after 4 H_2O-splitting cycles, indicating no appreciable changes in the local structural around zinc in 10Zn since the first cycle. Although the distribution of zinc within 10Zn after 4 H_2O-splitting cycles is inhomogeneous (Fig. 4 and 5), the average XAS spectra essentially do not differ from the ones collected in the Zn-rich region. As discussed earlier, the inhomogeneity of the zinc distribution is only due to the inhomogeneous distribution of the secondary ZnO phase, and the incorporation of zinc in the ceria lattice is homogeneous from a long-range order perspective (μ-XRD). With the XAS studies, we find no evidence suggesting any inhomogeneity in the local coordination environment around the Zn that is incorporated in the ceria lattice.

Thermochemical CO_2 splitting

To shed light on the cause of the significant loss of zinc during the first 4 H_2O-splitting cycles reported in Fig. 4, thermogravimetric analyses of native ceria and Zn-modified ceria for thermochemical CO_2 splitting were performed. The results are presented in Fig. 8. In each cycle the mass loss during thermal reduction at 1300 °C is significantly larger than the subsequent mass gain during reoxidation by CO_2 at 1000 °C for both Zn-modified samples. This is particularly true for the first two to three cycles. For example, in the first cycle, nearly 2% mass loss is observed for both 10Zn and 20Zn during reduction while the subsequent reoxidation shows almost no mass gain. This mismatch clearly reveals that the loss of zinc observed by XRF (Fig. 4) is caused by ZnO sublimation during the thermal reduction steps. The mass loss of native ceria during thermal reduction is caused

by thermal reduction of ceria to a non-stoichiometric phase. The mass loss is much smaller with respect to Zn-modified samples as no ZnO sublimation occurs in native ceria. The very gradual mass loss during the four cycles is attributed to the loss of a small amount of ZnO that diffused into the crucible during the experiments with 10Zn and 20Zn. In fact, the crucible itself showed a mass gain of about 1 mg after the experiments with 10Zn and 20Zn. Its weight returned to its starting value after experiment with native ceria. Taking a closer look at the reoxidation steps, *i.e.* the isothermal segments at 1000 °C, one notices that the mass gain (%), from which the CO produced is calculated, clearly increases with increasing number of cycles for both 10Zn and 20Zn, while it stays almost constant for native ceria. This is consistent with the H_2O-splitting results presented in Fig. 2 and 3.

A further evaluation of the materials for CO_2-splitting cycles was carried out with fresh samples. The temperature for thermal reduction was increased to 1400 °C to increase the extent of reduction. The results are presented in Fig. 9. For better comparison between cycles of a given material, the TGA profiles during the four reduction segments are grouped together and so are the ones during the corresponding reoxidation segments. Relative mass losses and gains are adjusted to zero when the temperature reaches 1000 °C (during heating) and at the beginning of each reoxidation segment, respectively. Clearly, mass loss is most significant in the initial cycle and then decreases in the following cycles for the Zn-modified samples. The initial mass losses are larger than the ones reported in Fig. 8. This is to be expected as the rate of sublimation is higher at 1400 °C than at 1300 °C. The TGA data presented in Fig. 8 and 9 confirm the XRF results that revealed a rapid decrease of the zinc content in the initial cycles. The larger mass loss observed for native ceria during the reduction segment in the first cycle is likely to be caused by the release of impurities or adsorbates at temperatures above 1000 °C. The following three reduction profiles overlap, indicating essentially identical amounts of oxygen released in each cycle. This is in agreement with the data obtained at the lower reduction temperature. For 20Zn and 10Zn, both MS data (low temperature cycles of Fig. 8) and GC data (high temperature cycles of Fig. 9) show only a small increase of oxygen evolution. This provides extra evidence supporting that the significant mass losses occurring in the first few cycles are not due to much higher degree of reduction but caused by ZnO sublimation. This interpretation is also confirmed by the reoxidation profiles. Native ceria exhibits nearly constant mass gains in the four cycles. The small increase observed is an artifact due to a drift in the buoyancy correction used. In comparison, the reoxidation profiles of 20Zn and 10Zn are clearly different. The significant increase of mass gain per cycle cannot be attributed to the buoyancy related artifact. It is caused by significantly increased oxygen uptake, which is proportional to the CO produced (see eqn (2b)). The observed increase of the CO produced is in excellent agreement with the H_2O-splitting results reported earlier. Moreover, the mass gain in the 4th cycle for 20Zn also seems to exceed the
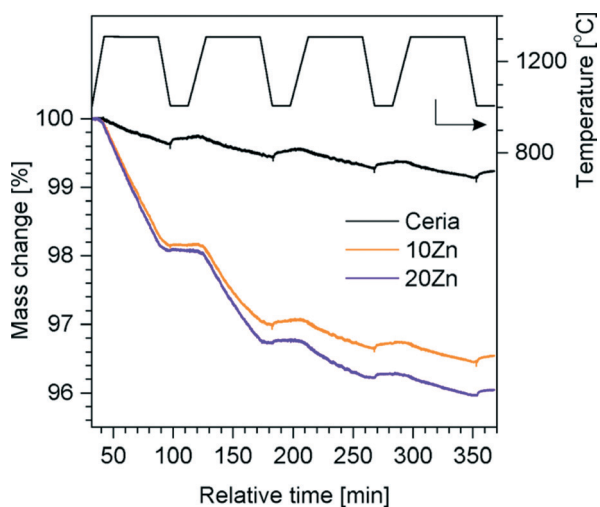

Fig. 8 TGA profiles of 4 CO_2-splitting cycles using native ceria, 10Zn, and 20Zn.
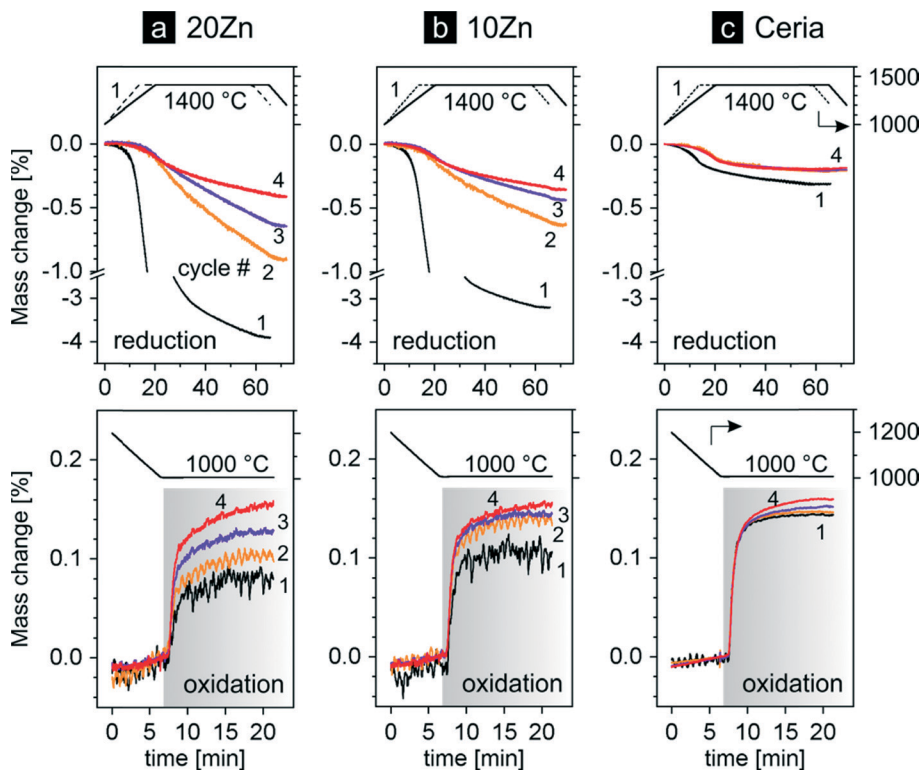
Fig. 9 TGA profiles of four thermochemical CO_2-splitting cycles with (a) 20Zn, (b) 10Zn and (c) native ceria. Top row: mass loss profiles during reduction at 1400 °C, and bottom row: mass gain profiles during reoxidation (grey region) at 1000 °C by CO_2.

average mass gain of native ceria, which is again consistent with earlier observations (Fig. 3).

Combining the results of XRF, XRD, XAS and activity tests, a clear picture of the physicochemical changes occurring in Zn-modified ceria during the initial cycles emerges and an in-depth understanding of their effect on the thermochemical activity can be established. Significant amounts of X-ray amorphous ZnO with local structure similar as ZnO nanoparticles (2.1 nm) are present in the fresh Zn-modified ceria material. This secondary phase is homogeneously distributed and difficult to detect by standard XRD. It crystalizes very quickly to bulk wurtzite ZnO during the first cycle when the material is exposed to high temperatures. As a result the zinc distribution becomes inhomogeneous. After repeated cycles most of the ZnO phase is lost through sublimation during the high temperature thermal reduction steps. Trace amounts of ZnO are still present after four cycles. Part of the zinc remaining in the material is incorporated in the ceria lattice, as least for 20Zn. The loss of the ZnO phase during the first few cycles is accompanied by a gradual increase of H_2O- and CO_2-splitting activities of the material. This suggests that the presence of the ZnO phase is detrimental to the thermochemical activity of Zn-modified ceria. It seems to hinder slightly the release of oxygen during thermal reduction and significantly the reoxidation of the activated ceria by H_2O and CO_2. Once the majority of the ZnO is lost through sublimation, the activity of Zn-modified ceria slightly surpasses the activity of native ceria. The increased OSC due to

the zinc remaining incorporated in the ceria lattice after the initial cycles is considered to be responsible for the observed higher thermochemical activity of the Zn-modified material.

Lastly, while the enhancement of the activity of ceria-based materials is one of the important factors that determine the economic viability of solar fuel production by thermochemical cycles on an industrial scale, many studies only present results of very few cycles. However, it is imperative to investigate the material's long-term activity since any effort to promote the material's activity for only a few cycles is meaningless if the material rapidly degrades. In first attempt to assess its long-term activity, Zn-modified ceria was tested for 12 CO_2-splitting cycles using the TGA (same condition as presented in Fig. 9). Three consecutive runs with four cycles each were performed. The CO productivity was calculated based on the mass gain during each isothermal reoxidation segment and the active sample mass. To take into account the mass loss due to the sublimation of ZnO, the mass of active material used in the calculation was determined at the end of the experiment. The identical buoyancy correction for four cycles was applied in each run. The results are presented in Fig. 10. The small but consistent increase of the CO produced, clearly visible during the 2nd and the 3rd run of Zn-modified ceria as well as during the first and the only run of native ceria, is an artifact due to the drift in the buoyancy correction as discussed earlier. However, the much larger increase observed in the first run of 10Zn and of 20Zn is mainly due to genuine increase of CO produced. Neglecting the
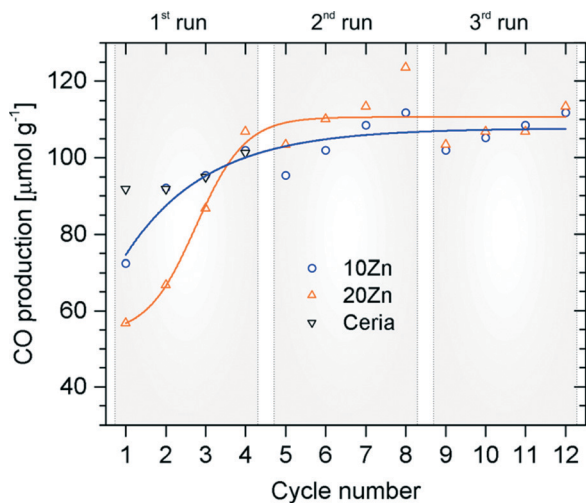
Fig. 10 CO production per gram of materials during 12 CO_2-splitting cycles (three consecutive runs with four cycles per run) with reoxidation at 1000 °C and thermal reduction at 1400 °C.

artifact, it appears that the activity of native ceria is quite stable from the beginning while the activity of Zn-modified ceria stabilizes after 4–6 cycles at levels exceeding that of native ceria. The amounts of CO produced by 20Zn and by 10Zn per cycle increase from 56 μmol g^{-1} to over 110 μmol g^{-1} and from 72 μmol g^{-1} to 107 μmol g^{-1}, respectively. The values for native ceria are relatively constant and in the range of 90 to 95 μmol g^{-1}.

Conclusions

Zn-modified ceria has been evaluated as a redox material for H_2O splitting and CO_2 splitting by solar-driven thermochemical cycles (STCs). Contrary to a typical decrease of thermochemical activity due to sintering, the amounts of H_2 and CO produced increase significantly during the initial few cycles. The H_2 and CO productivities eventually seem to stabilize and exceed that of native ceria. To elucidate the unexpected change in activity, we have combined traditional and advanced techniques to unravel the physicochemical changes of the material that occur during these initial cycles. The significant amounts of X-ray amorphous ZnO present in the fresh Zn-modified ceria material, revealed in a previous study and confirmed by XAS here, are not stable at thermal reduction temperatures up to 1400 °C. This secondary ZnO phase quickly crystallizes in the first cycle according to XAS, and the majority of this phase is lost in the first four cycles by sublimation according to XRF and TGA. The firstly rapid and then gradual loss of the secondary ZnO phase in the initial cycles correlates well with the observed significant increase of H_2 and CO productivities, strongly indicating a detrimental effect of the secondary ZnO phase on the thermochemical activity of Zn-modified ceria. According to synchrotron μ-XRD, small amounts of ZnO are still present in the material after 4 H_2O-splitting cycles, and part of the zinc that remains in the material is incorporated in the ceria lattice. The increased OSC due to the zinc remaining incorporated is considered to be

responsible for the eventually higher thermochemical activity of the Zn-modified ceria material. In addition, by combining μ-XRD and μ-XAS with μ-XRF, we are able to reveal a homogeneous distribution of the zinc that remains incorporated in the ceria lattice after the initial cycles. The inhomogeneity in the zinc element distribution is solely due to an inhomogeneous distribution of the secondary ZnO phase.

As concluding remarks, although the results of the 12 CO_2-splitting cycles presented is encouraging, the long-term thermochemical activity of the material needs to be further evaluated. In addition, the local coordination environment around the zinc incorporated in the ceria lattice remains to be fully elucidated. However, this study clearly stresses the importance of unravelling the physicochemical changes of the redox material during the STCs in order to understand its activity and design better-performing materials. Together with a previous study of the same material, this study also underlines the necessity to evaluate the material's structural and chemical stability at the conditions of STCs, if a catalyst designed for reactions at low-to-moderate temperatures is considered as a redox material for STCs.

Acknowledgements

References

1 N. S. Lewis and D. G. Nocera, *Proc. Natl. Acad. Sci. U. S. A.*, 2006, **103**, 15729–15735.
2 IEA (International Energy Agency), *World Energy Outlook 2014*, OECD/IEA, Paris, 2014.
3 J. R. Scheffe, D. Weibel and A. Steinfeld, *Energy Fuels*, 2013, **27**, 4250–4257.
4 A. Demont, S. Abanades and E. Beche, *J. Phys. Chem. C*, 2014, **118**, 12682–12692.
5 A. H. McDaniel, E. C. Miller, D. Arifin, A. Ambrosini, E. N. Coker, R. O'Hayre, W. C. Chueh and J. Tong, *Energy Environ. Sci.*, 2013, **6**, 2424–2428.
6 A. Demont and S. Abanades, *RSC Adv.*, 2014, **4**, 54885–54891.
7 A. Demont and S. Abanades, *J. Mater. Chem. A*, 2015, **3**, 3536–3546.
8 C.-K. Yang, Y. Yamazaki, A. Aydin and S. M. Haile, *J. Mater. Chem. A*, 2014, **2**, 13612–13623.
9 Q. Jiang, J. Tong, G. Zhou, Z. Jiang, Z. Li and C. Li, *Sol. Energy*, 2014, **103**, 425–437.
10 S. Dey, B. S. Naidu, A. Govindaraj and C. N. R. Rao, *Phys. Chem. Chem. Phys.*, 2015, **17**, 122–125.
11 S. Dey, B. S. Naidu and C. N. R. Rao, *Chem. – Eur. J.*, 2015, **21**, 7077–7081.
12 J. R. Scheffe and A. Steinfeld, *Mater. Today*, 2014, **17**, 341–348.

13 J. E. Miller, A. H. McDaniel and M. D. Allendorf, *Adv. Energy Mater.*, 2014, **4**, 1300469.

14 W. C. Chueh and S. M. Haile, *Philos. Trans. R. Soc., A*, 2010, **368**, 3269–3294.

15 W. C. Chueh, C. Falter, M. Abbott, D. Scipio, P. Furler, S. M. Haile and A. Steinfeld, *Science*, 2010, **330**, 1797–1801.

16 P. Furler, J. Scheffe and A. Steinfeld, *Energy Environ. Sci.*, 2012, **5**, 6098–6098.

17 P. Furler, J. Scheffe, D. Marxer, M. Gorbar, A. Bonk, U. Vogt and A. Steinfeld, *Phys. Chem. Chem. Phys.*, 2014, **16**, 10503–10511.

18 S. Ackermann, J. R. Scheffe and A. Steinfeld, *J. Phys. Chem. C*, 2014, **118**, 5216–5225.

19 H. Kaneko, T. Miura, H. Ishihara, S. Taku, T. Yokoyama, H. Nakajima and Y. Tamaura, *Energy*, 2007, **32**, 656–663.

20 S. Abanades, A. Legal, A. Cordier, G. Peraudeau, G. Flamant and A. Julbe, *J. Mater. Sci.*, 2010, **45**, 4163–4173.

21 A. Le Gal and S. Abanades, *Int. J. Hydrogen Energy*, 2011, **36**, 4739–4748.

22 A. Le Gal, S. Abanades and G. Flamant, *Energy Fuels*, 2011, **25**, 4836–4845.

23 A. Le Gal and S. Abanades, *J. Phys. Chem. C*, 2012, **116**, 13516–13523.

24 S. Abanades and A. Le Gal, *Fuel*, 2012, **102**, 180–186.

25 A. Le Gal, S. Abanades, N. Bion, T. Le Mercier and V. Harle, *Energy Fuels*, 2013, **27**, 6068–6078.

26 C.-I. Lee, Q.-L. Meng, H. Kaneko and Y. Tamaura, *J. Sol. Energy*, 2013, **135**, 011002.

27 J. R. Scheffe, R. Jacot, G. R. Patzke and A. Steinfeld, *J. Phys. Chem. C*, 2013, **117**, 24104–24114.

28 M. Kang, J. Zhang, C. Wang, F. Wang, N. Zhao, F. Xiao, W. Wei and Y. Sun, *RSC Adv.*, 2013, **3**, 18878–18885.

29 M. Kang, X. Wu, J. Zhang, N. Zhao, W. Wei and Y. Sun, *RSC Adv.*, 2014, **4**, 5583–5590.

30 Q.-L. Meng, C.-I. Lee, T. Ishihara, H. Kaneko and Y. Tamaura, *Int. J. Hydrogen Energy*, 2011, **36**, 13435–13441.

31 G. Avgouropoulos, M. Manzoli, F. Boccuzzi, T. Tabakova, J. Papavasiliou, T. Ioannides and V. Idakiev, *J. Catal.*, 2008, **256**, 237–247.

32 O. H. Laguna, M. A. Centeno, F. Romero-Sarria and J. A. Odriozola, *Catal. Today*, 2011, **172**, 118–123.

33 S.-L. Zhong, L.-F. Zhang, L. Wang, W.-X. Huang, C.-M. Fan and A.-W. Xu, *J. Phys. Chem. C*, 2012, **116**, 13127–13132.

34 F. Lin, I. Alxneit and A. Wokaun, *CrystEngComm*, 2015, **17**, 1646–1653.

35 F. Lin, R. Delmelle, T. Vinodkumar, B. M. Reddy, A. Wokaun and I. Alxneit, *Catal. Sci. Technol.*, 2015, **5**, 3556–3567.

36 F. Lin, A. Wokaun and I. Alxneit, *Energy Procedia*, 2015, **69**, 1790–1799.

37 K. Schmale, M. Daniels, A. Buchheit, M. Gruenebaum, L. Haase, S. Koops and H. D. Wiemhoefer, *J. Electrochem. Soc.*, 2013, **160**, F1081–F1087.

38 A. Patlolla, J. Zunino, A. I. Frenkel and Z. Iqbal, *J. Mater. Chem.*, 2012, **22**, 7028–7035.

39 I. Perelshtein, E. Ruderman, N. Perkas, T. Tzanov, J. Beddow, E. Joyce, T. J. Mason, M. Blanes, K. Molla, A. Patlolla, A. I. Frenkel and A. Gedanken, *J. Mater. Chem. B*, 2013, **1**, 1968–1976.

40 A. Kuzmin and J. Chaboy, *IUCrJ*, 2014, **1**, 571–589.